Multimodal Magneto-Plasmonic Nanoclusters for Biomedical Applications

*Chun-Hsien Wu, Jason Cook, Stanislav Emelianov, and Konstantin Sokolov**

Multimodal nanostructures can help solve many problems in the biomedical field including sensitive molecular imaging, highly specific therapy, and early cancer detection. However, the synthesis of densely packed, multicomponent nanostructures with multimodal functionality represents a significant challenge. Here, a new type of hybrid magneto-plasmonic nanoparticles is developed using an oil-in-water microemulsion method. The nanostructures are synthetized by self-assembly of primary 6 nm iron oxide core-gold shell particles resulting into densely packed spherical nanoclusters. The dense packing of primary particles does not change their superparamagnetic behavior; however, the close proximity of the constituent particles in the nanocluster leads to strong near-infrared (NIR) plasmon resonances. The synthesis is optimized to eliminate nanocluster cytotoxicity. Immunotargeted nanoclusters are also developed using directional conjugation chemistry through the Fc antibody moiety, leaving the Fab antigen recognizing region available for targeting. Cancer cells labeled with immunotargeted nanoclusters produce a strong photoacoustic signal in the NIR that is optimum for tissue imaging. Furthermore, the labeled cells can be efficiently captured using an external magnetic field. The biocompatible magneto-plasmonic nanoparticles can make a significant impact in development of point-of-care assays for detection of circulating tumor cells, as well as in cell therapy with magnetic cell guidance and imaging monitoring.

1. Introduction

The field of nanotechnology provides opportunities for the development of hybrid nanomaterials which can enable new approaches and methods in various biomedical applications including molecular imaging and therapy.[1] During the past few years, the combination of materials with magnetic and plasmonic properties on nanoscale has drawn particular interest due to their unique characteristics.[2] Indeed, gold-based nanoparticles exhibit strong localized surface plasmon resonances in visible and near-infrared (NIR) spectral regions; this property has been explored in a plethora of exciting applications ranging from molecular imaging to photothermal therapy and drug release.[3] Similarly, superparamagnetic nanoparticles are of great interest because of their applications in cell and molecular separation assays; magneto-motive optical and ultrasound imaging; magnetic resonance imaging (MRI); and hyperthermia cancer treatment.[4]

Recent reports have demonstrated a synergistic potential of combining plasmonic and superparamagnetic nanoparticles.[5] For example, spherical gold shell/iron oxide core nanoparticles were used for molecular optical and MRI imaging in combination with photothermal therapy of cancer cells overexpressing epidermal growth factor receptor (EGFR).[5a] In another study, gold shell/iron oxide core nanoparticles enabled a highly sensitive magneto-motive dark-field optical imaging of cancer cells.[6] In this case, the combination of bright plasmon resonance scattering from the gold shell and modulation of the optical signal by an external magnetic field was used to significantly increase imaging contrast. The same approach was used for the detection of single stellated gold nanoparticles containing a magnetic iron oxide core, demonstrating high sensitivity of this imaging approach.[5c] More recently, magneto-plasmonic nanoparticles were used in the development of a new imaging approach—magneto-photoacoustic imaging—that increases imaging contrast in cellular and molecular imaging at significant tissue depth.[4b,7]

One emerging application of magneto-plasmonic nanomaterials is a simultaneous capture and detection of circulating tumor cells (CTCs). In initial experiments, two separate functionalized nanoparticles were used – magnetic iron oxide particles for cell capture and gold-plated carbon nanotubes for photoacoustic (PA) detection of the captured CTCs.[8] These experiments showed the feasibility of capture and detection of breast cancer cells pre-injected into a mouse bloodstream in vivo. However, the use of two different nanoparticles for the capture and detection of CTCs can significantly limit the efficacy of this approach because of the limited number of specific biomarkers overexpressed in cancer, and the associated problem

Dr. C.-H. Wu, Dr. J. Cook, Prof. S. Emelianov, Prof. K. Sokolov
Department of Biomedical Engineering
University of Texas at Austin
Austin, TX, 78712, USA
E-mail: ksokolov@mdanderson.org
Dr. C.-H. Wu, Prof. K. Sokolov
Department of Imaging Physics
University of Texas M.D. Anderson Cancer Center
Houston, TX, 77030, USA

DOI: 10.1002/adfm.201401806

of finding two different biomarkers specific for each cancer type. Therefore, the latest approaches in this field have utilized hybrid magneto-plasmonic nanoparticles.[9] Silica-coated gold nanorods adorned with iron-oxide nanoparticles and conjugated with folic acid molecules were used to demonstrate the feasibility of capture and PA detection of pre-labeled and fixed HeLa cancer cells under flow conditions.[9b] In another study, our group synthesized immunotargeted 6 nm iron oxide shell/gold core nanoparticles for capture of skin, breast and colon cancer cells in whole blood without any pre-processing steps using a permanent magnet and a flow chamber.[9a] We demonstrated a capture efficiency greater than 90% when a mixture of two nanoparticles targeted to two cancer biomarkers was used.[9a]

Although previous studies have shown the potential of hybrid magneto-plasmonic nanoparticles, significant limitations have been also uncovered. The use of gold nanorods as a template for the deposition of iron oxide nanoparticles requires careful optimization to ensure colloidal stability. Furthermore, there is significant variability in the number of iron oxide moieties per hybrid nanoparticle because of the limited nanorod surface area (transmittance electron microscopy (TEM) shows less than 10 iron oxide particles per nanorod).[9b] The 6 nm diameter core/shell nanoparticles have a relatively small magnetic moments and exhibit plasmon resonance at ≈520 nm, where whole blood has strong absorbance.[9a] The latter limitation is overcome when spherical plasmonic nanoparticles are targeted to an overexpressed cancer biomarker or when they undergo an endosomal uptake by cancer cells; in this case, the effect of plasmon resonance coupling between closely spaced nanoparticles results in a strong broadband absorbance that extends to the NIR.[3a,10] However, the effect of surface plasmon resonance coupling is not likely to be observed for all cancer biomarkers of interest. Alternatively, core-shell magneto-plasmonic nanostructures with a strong NIR absorbance were synthesized by attaching a layer of a positively charged poly-L-histidine or aminosilane molecules on a magnetic core nanoparticle followed by deposition of a gold shell.[7,11] However, uneven or low polymer coverage on the magnetic core can compromise the deposition of a gold shell. Furthermore, this approach results in magneto-plasmonic nanoparticles with a single superparamagnetic moiety thus limiting the magnetic moment of the hybrid nanoparticles. It was shown that the latter limitation can be overcome in a one-pot reaction which combines hydroxylamine mediated deposition of gold on 5 nm dextran-coated iron oxide nanoparticles with a concurrent kinetically controlled particle aggregation.[12] Although this procedure results in ≈30 nm diameter nanoparticles with superparamagnetic properties and a strong NIR absorbance, the nanoparticles exhibit high variability in shape and gold-to-iron oxide ratio. Furthermore, TEM showed presence of iron oxide clusters that are not coated by a gold shell in nanoparticle preparations.[13] Therefore, better methods for synthesis of hybrid nanoparticles with a high magnetic moment and strong absorbance in the red–NIR spectral region are needed.

Here, we address this need with the development of a new type of hybrid magneto-plasmonic nanostructures using oil-in-water microemulsion method.[14] The nanostructures are synthetized from hybrid primary 6 nm iron oxide core-gold shell nanoparticles which self-assemble into dense spherical nanoclusters. After the primary nanoparticles are made, the nanocluster synthesis is essentially a simple one-pot reaction. The use of hybrid primary particles ensures consistent proportions of magnetic (iron oxide) and plasmonic (gold) moieties in the resulting nanoclusters. We demonstrated that the dense packing of the hybrid primary particles did not change their superparamagnetic properties and, therefore, the overall magnetic moment of the nanoclusters is not limited by the size transition of iron oxide from superparamagnetism to ferrimagnetism.[15] Furthermore, the close proximity of the primary particles advantageously resulted in a strong red–NIR absorbance which is well suited for imaging and therapeutic applications in vivo. Thus, our approach provides the combination of a facile synthesis, tunability of magnetic moment without sacrificing superparamagnetic properties, and strong visible-NIR absorbance, thus addressing major limitations of previous synthetic methods.

We demonstrated that the magneto-plasmonic nanoclusters provide strong contrast in PA imaging and can be used for the magnetic separation of labeled cells. The nanoclusters were conjugated with monoclonal antibodies specific for two major cancer biomarkers—epidermal growth factor receptors 1 and 2 (EGFR and HER2, respectively)[16]—using directional conjugation chemistry.[17] The molecularly targeted nanoclusters demonstrated drastically improved magnetic capture and high PA imaging sensitivity of labeled cancer cells, when compared to primary core-shell magneto-plasmonic particles. Overall, the hybrid nanoclusters described here exhibit the combination of properties which can allow transition from highly promising feasibility studies to actual translation of magneto-plasmonic nanoparticles to a variety of biomedical applications.

2. Results and Discussion

Oil-in-water microemulsion has been demonstrated as a versatile method to prepare single material nanoclusters with high colloidal stability.[14] Size, composition, and surface charge of the nanoclusters are controllable and tunable by choosing primary metal nanoparticles and surfactants.[14a] Several types of nanoclusters have been successfully synthesized and characterized by using magnetic (Fe_3O_4), plasmonic (Au), or semiconductor (CdS) primary nanoparticles.[14b] Here, we extended this microemulsion approach to the synthesis of novel hybrid nanostructures with dual magneto-plasmonic properties (**Figure 1**). Nanocluster formation requires amphiphilic surfactants with a hydrophobic moiety to hold together the primary particles inside the cluster, through hydrophobic van der Waals interactions, and a polar group to provide aqueous solubility. There are many surfactants that can be used for this purpose such as cationic surfactants (e.g., cetyltrimethylammonium bromide (CTAB)), anionic surfactants (e.g., sodium dodecyl sulfate (SDS)), nonionic surfactants (e.g., Triton X-100), and polymers (e.g., polyethyleneimine). The surfactant choice depends on the application. In our case, we chose anionic SDS molecules because they result in nanoclusters with enhanced biocompatibility and can be easily replaced with methyl-PEG-thiol (mPEG-SH) molecules, as shown below.

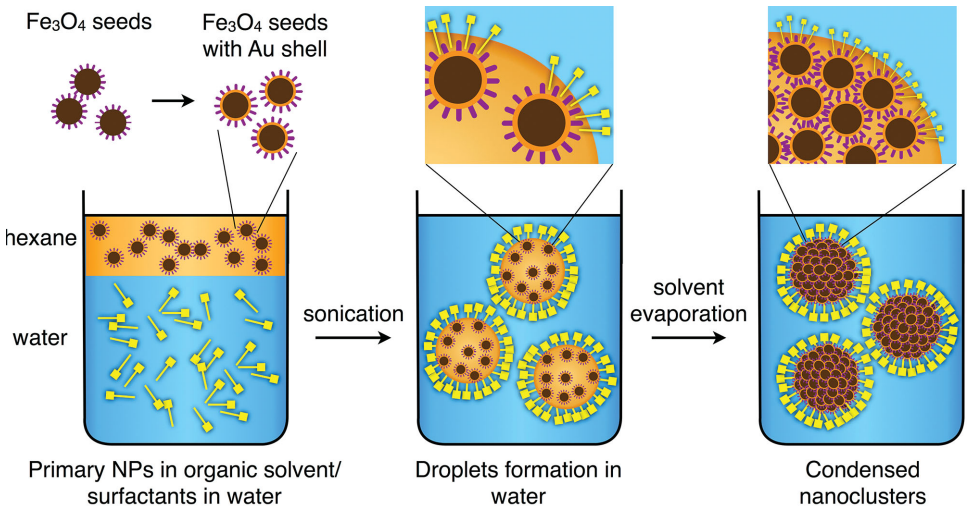

Figure 1. The synthesis scheme of the magneto-plasmonic nanoclusters by utilizing an oil-in-water microemulsion method.

First, primary iron oxide core/gold shell nanoparticles were prepared via the thermal decomposition method.[18] Analysis of TEM images showed that after gold deposition size distribution of the primary nanoparticles is shifted by 1 nm without changes in the standard deviation (5.1 ± 0.8 nm and 6.2 ± 0.8 nm for iron oxide and iron oxide core/gold shell primary particles, respectively) that indicates consistent thickness of the gold shell (Figure S1, Supporting Information). The resultant oleic acid-capped core/shell nanoparticles have high monodispersity with a 6.2 ± 0.8 nm diameter and are readily dispersed in hexane (**Figure 2**A). In a typical nanocluster synthesis, a suspension of the core/shell primary nanoparticles in hexane was carefully added to an aqueous solution containing anionic SDS surfactants with a hexane-to-water ratio of 1:10 by volume. The nanoclusters were formed under ultrasound treatment at the interfacial layer between the two immiscible phases. During this process the amphiphilic SDS surfactants from the aqueous phase undergone hydrophobic van der Waals interactions with the hydrocarbon tail of oleic acids, which stabilized the primary nanoparticles in hexane. Meanwhile, the hydrophilic head groups of SDS molecules interact with the aqueous phase acting as stabilizing agents and preventing aggregation of the forming nanoclusters (Figure 1). Subsequent heating of the reaction mixture above the boiling temperature of hexane resulted in hexane evaporation and the final formation of magneto-plasmonic nanoclusters with densely packed primary particles (Figure 2B).

Scanning electron microscopy (SEM) indicates that primary particles retained their individual character and served as building blocks in nanocluster formation (Figure 2C). As-synthesized nanoclusters had a wide size distribution from several nanometers to ≈300 nm. Various size fractions were separated by a gradient centrifugation (Figure S2, Supporting Information). Figure 2D shows size distribution of nanoclusters with sizes 180 ± 39 nm as determined by TEM measurements of ≈200 particles. This nanocluster size was selected for thorough evaluation because of its significantly stronger NIR absorbance, as compared to smaller nanoclusters (Figure S2, Supporting Information). There were pronounced differences in the absorbance spectra of nanoclusters and primary nanoparticles (Figure 2E); the spectra were obtained for suspensions with the same mass of Au as determined by inductively coupled plasma mass spectrometry (ICP-MS). Note that in this experiment the molar concentration of nanoclusters is almost four orders of magnitude less than the concentration of the primary particles because each nanocluster consists of many primary particles. Therefore, even though the absorbance cross-section of nanoparticles is expected to increase with size[19] the lower molar concentration of nanoclusters results in an overall decrease in the absorbance in the UV–Vis spectral range. Similar behavior during transition from isolated to aggregated nanoparticles has been observed before.[20] Purple colloidal suspension of primary core/shell nanoparticles showed a distinctive absorbance peak at 538 nm, which is characteristic of isolated core/shell spheres. The grey nanocluster dispersion had a broad absorbance in the NIR region (Figure 2F), which can be attributed to a plasmon resonance coupling between the closely spaced primary particles. The inter-particle gaps are a fraction of the primary particle diameter, thereby resulting in broadening and a red–NIR shift in the absorbance of the nanoclusters.[14b,21] However, it is interesting to note that the NIR absorbance is increasing gradually with increase in nanocluster sizes (Figure S2, Supporting Information). A pronounced increase in the NIR absorbance for the larger nanoclusters could be associated with a significant difference in optical properties of primary particles that are located on the surface versus particles located in the inner nanocluster core, which becomes more pronounced as size increase.[10b,22] However, a thorough theoretical analysis would need to be carried out in order to get a better understanding of the optical behavior of these composite nanoclusters, which is outside the scope of this study.

Magnetic properties of nanoclusters were characterized using SQUID (superconducting quantum interference device) magnetometry by cycling the field magnetic field between +10 and −10 K Oe at 300 K. Neither coercivity nor remanence was observed, indicating superparamagnetic properties of both the primary particles and the nanoclusters (**Figure 3**A). The nanoclusters and the primary particles exhibited similar

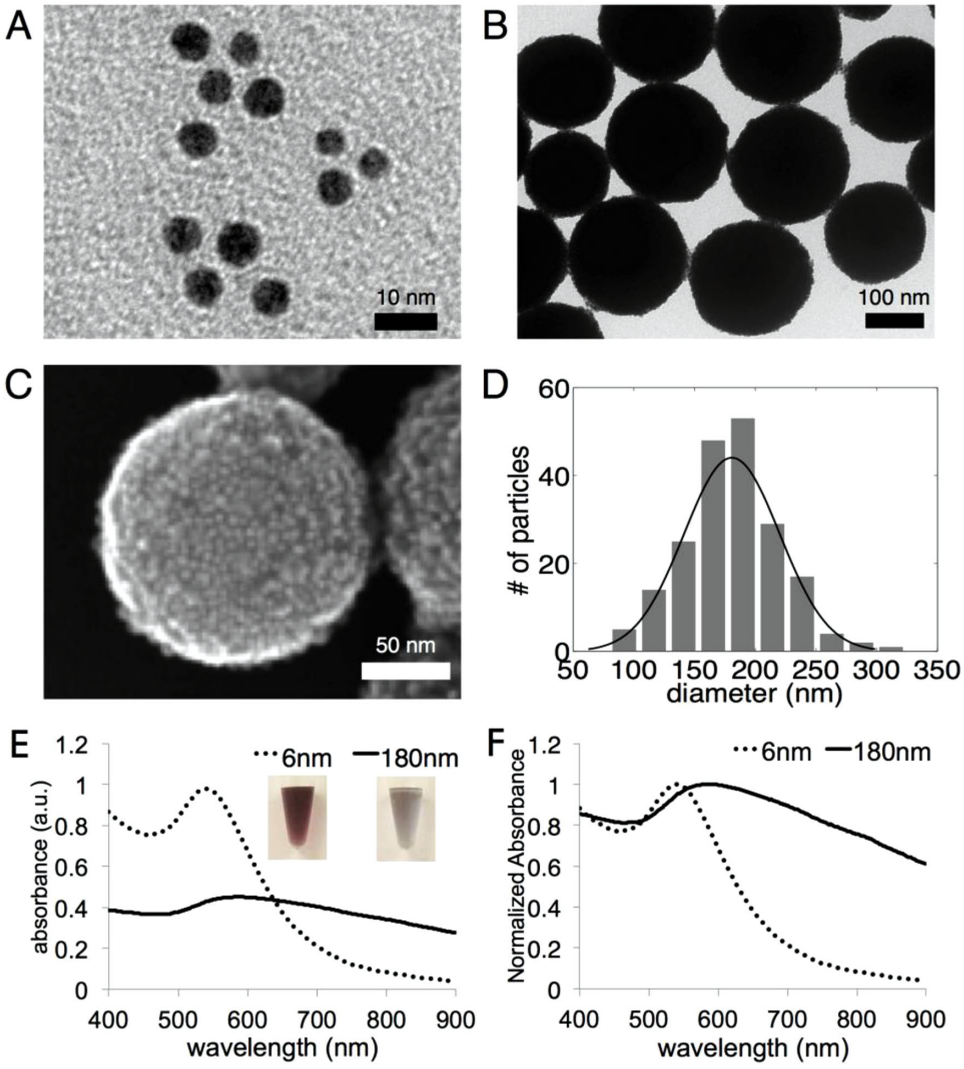

Figure 2. Characterization of magneto-plasmonic nanoclusters. A) TEM image of primary gold shell/Fe_3O_4 core nanoparticles. B–D) TEM image, SEM image and size distribution of ≈180 nm diameter magneto-plasmonic nanoclusters, respectively; the size distribution was determined from TEM image analysis by counting more than 200 particles. E) UV–Vis spectra of primary particles (dotted line) and nanoclusters (solid line) with the same mass of Au; the insert in (E) shows changes in colloid color from red for primary particles to purple-grey for nanoclusters. F) Normalized absorbance spectra from (E).

magnetization, indicating that the constituent particles are separated inside the nanoclusters. The small ≈1.85 emu/g increase in the magnetization of nanoclusters can be attributed to a cooperativity effect between closely spaced iron oxide cores.[23] Because the magnetic force acting on a nanocluster is proportional to the number of primary particles, the nanoclusters exhibited an improved response to an external magnet (Figure 3B,C). A suspension of either primary particles or nanoclusters was placed next to a permanent magnet in a cuvette with a 1 cm pathlength, and the depletion of the nanoparticles from each dispersion was measured using UV–Vis spectrophotometry. The initial absorbance (no magnet) at 590 nm for nanoclusters and 538 nm for primary particles gave 100% of the total amount of nanoparticles. After 5 min magnetic incubation, the nanocluster solution was depleted 53% versus a 7% for the primary particles (Figure 3B,C). After 15 min incubation, 73% of nanoclusters and 16% of primary particles were captured by the magnet. Therefore, the use of nanoclusters results in a significantly increased magnetic force while preserving superparamagnetic properties of the nanoparticles.

It has been shown that biocompatibility of plasmonic nanoparticles is highly dependent on their surface coating.[24] Several strategies can be employed to ensure nanoparticle biocompatibility, including the use of biocompatible surfactants during particle synthesis or the conjugation of biocompatible molecules on nanostructures after their synthesis. Here, we characterized the cellular toxicity of nanoclusters synthetized using CTAB and SDS capping ligands, as well as nanoclusters prepared by replacing SDS ligands with mPEG-SH molecules. Zeta potentials of the CTAB and SDS-capped nanoclusters were +48.5 ± 0.3 mV and −47.6 ± 6.0 mV, respectively (Table S1, Supporting Information). SDS replacement with

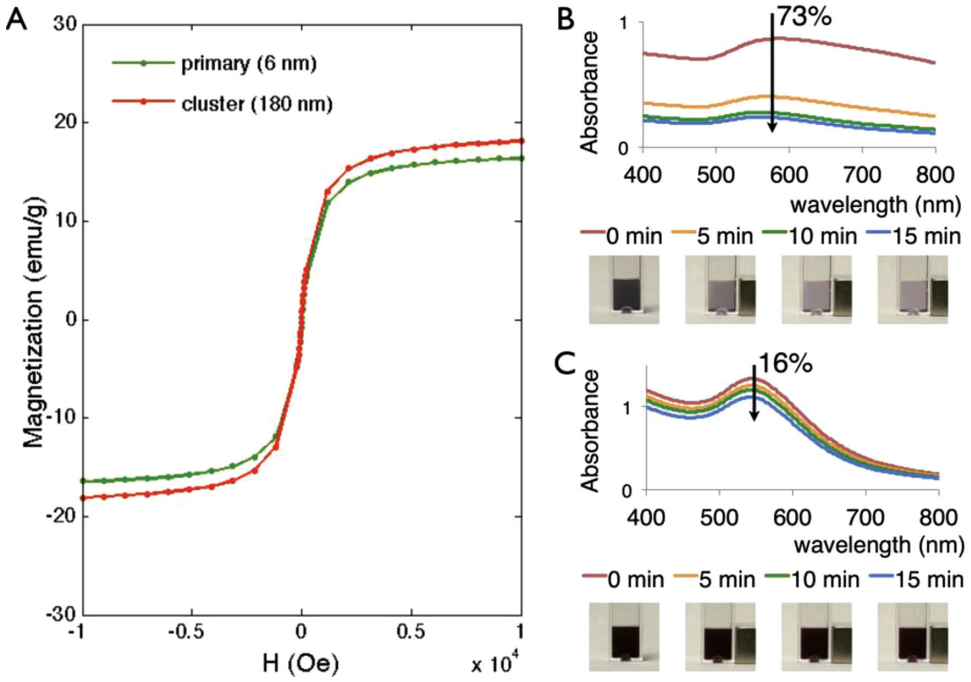

Figure 3. Characterization of magnetic properties of nanoclusters. A) Magnetization hysteresis at 300 K of primary particles and nanoclusters. B,C) Efficiency of magnetic separation of nanoclusters (B) and primary particles (C) from a colloidal aqueous suspension in a 1 cm cuvette in the presence of a permanent magnet. The yield (%) represents the portion of nanoparticles attracted to the magnet after 15 min magnet incubation as determined by the following formula: (1 – ([peak absorbance of magnet-treated sample]/[peak absorbance control sample without a magnet])) × 100%. The photographs show changes in turbidity of colloidal suspensions over time.

mPEG-SH molecules resulted in a nearly neutral surface charge of +3.3 ± 2.6 mV, indicating successful ligand exchange. Cell viability studies were performed using the A-431 cancer cell line (Figure S3, Supporting Information). Cell viability decreased by 80% and 65% after exposure to CTAB and SDS capped nanoclusters (particle concentration = 0.05 nM), respectively. Replacement of SDS with mPEG-SH molecules resulted in nanoclusters which did not show any cytotoxic effects. These results are consistent with previous reports where CTAB coated nanoparticles exhibited high cytotoxicity.[25] Similarly, SDS molecules are widely used to linearize proteins in SDS-PAGE (sodium dodecyl sulfate polyacrylamide gel electrophoresis) and, therefore, can adversely affect the function of many proteins.[26] These results indicate that SDS is a preferable agent for nanocluster synthesis as it reduces cytotoxic effects that are associated with CTAB. However, a ligand exchange of SDS with mPEG is required in order to render non-cytotoxic nanoclusters.

Nanoclusters were conjugated with monoclonal antibodies for molecular specific targeting of cancer cells. We used a directional covalent attachment of antibodies to the gold surface of the nanoclusters, leaving antigen binding sites on the Fab antibody region directed outward from the surface and therefore available for targeting.[17] Briefly, a carbohydrate moiety on Fc antibody portion was first oxidized to an aldehyde group using sodium periodate. Then a heterobifunctional polyethylene glycol linker, terminated at one end by a hydrazide moiety and di-thiol group at the other end, was attached to the oxidized carbohydrates on the antibody via its hydrazide portion, which resulted in a stable hydrazone bond with aldehydes. The modified antibodies were attached to the nanoclusters through the di-thiol portion of the linker. Subsequently, mPEG-SH molecules were added to passivate the rest of the exposed surface to ensure biocompatibility of the molecular targeted nanoclusters (**Figure 4**). A red shift of ≈32 nm of the absorbance peak of the nanoclusters was observed after the antibody conjugation, which indicates an increase in the local dielectric constant and, therefore, successful protein conjugation on the surface of nanoclusters (Figure S4, Supporting Information).[17] Furthermore, the attachment of clone 225 monoclonal EGFR antibodies resulted in a negative zeta potential of –7.0 ± 1.4 mV; a similar trend was previously reported for gold nanoparticles conjugated with antibodies.[25]

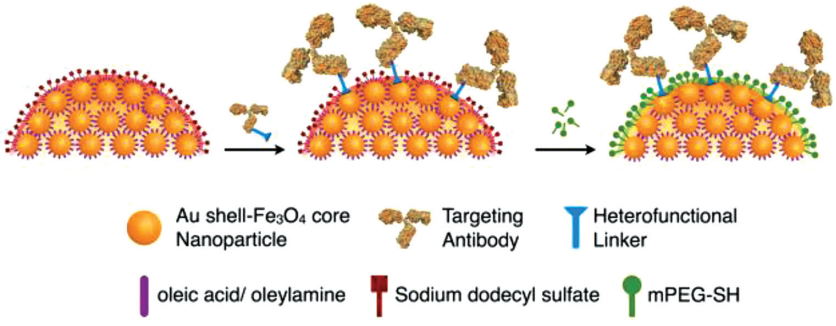

Figure 4. Schematic of the antibody conjugation to the nanoclusters through the antibody's Fc moiety using a hetero-functional linker.

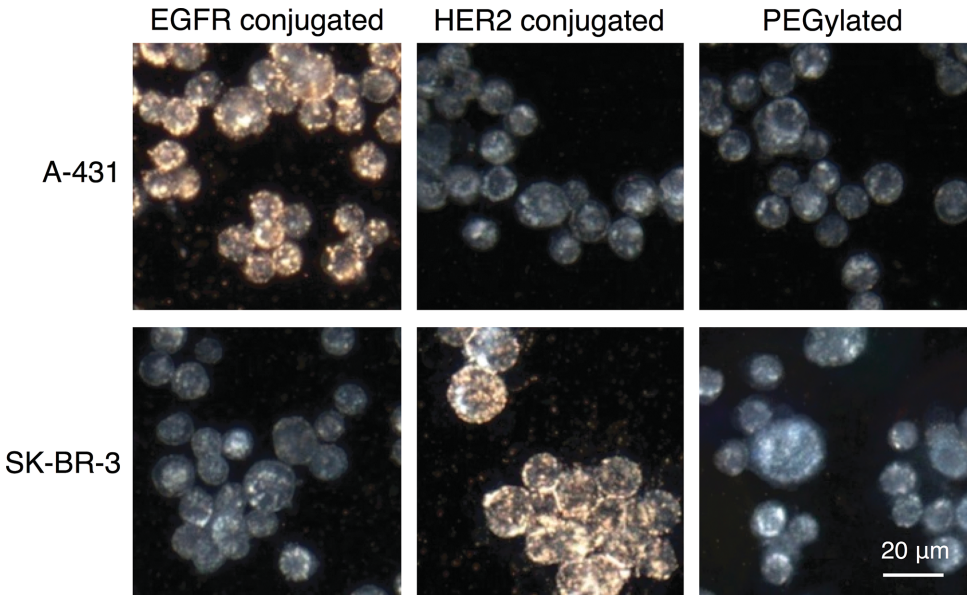

Figure 5. Dark-field reflectance images of cancer cells labeled with nanoclusters. Rows correspond to cancer cell with the following expression profiles: A-431(EGFR+/HER2–) and SK-BR-3 (EGFR–/HER2+). Columns show labeling results obtained with nanoclusters conjugated with anti-EGFR antibodies, anti-HER2 antibodies or mPEG molecules. The yellow-orange color in the darkfield images is associated with nanocluster binding; unlabeled cells have a characteristic grey-bluish appearance.

Molecular specificity of targeted nanoclusters was tested in two cell lines: 1) A-431 keratinocytes which express a high level of EGFR and are negative for epidermal growth factor receptor-2 (HER2), and 2) SK-BR-3 breast cancer cells which are negative for EGFR expression and positive for HER2. Nanoclusters targeted to either EGFR or HER2 and non-targeted PEGylated clusters were incubated with both cell types (**Figure 5**). Dark field microscopy images showed a bright orange color that is associated with light scattering from the nanoclusters for both the A-431 and SK-BR-3 cells incubated with EGFR and HER2 targeted nanoclusters, respectively. In contrast, cells exhibited characteristic bluish-gray color due to intrinsic cellular scattering after incubation with either targeted nanoparticles that did not match their expression profile or with PEGylated nanoclusters. Therefore, these results demonstrate molecular specificity of immunotargeted nanoclusters.

Next, we compared the optical properties of cells labeled with either primary particles or nanoclusters, which were both targeted to EGFR molecules (**Figure 6**). The same mass of gold was used for each nanoparticle type in cell labeling experiments. Labeling with EGFR-targeted nanoclusters resulted in a greatly increased absorbance of the A-431 cells when compared to anti-EGFR primary particles (Figure 6A). This data demonstrates the advantage of using bigger nanoparticles with higher absorbances for molecular specific cellular imaging; this is not necessarily a trivial result as the use of a bigger particle could result in a steric hindrance in labeling of closely spaced overexpressed molecules. Normalized absorbance spectra showed broadening and an increase in the red–NIR spectral region of nanoparticles that are interacting with cells, compared to isolated particles in a suspension (Figure 6B). These spectral changes can be attributed to the surface plasmon resonance coupling between nanoparticles which are brought in close proximity through their interactions with cellular EGFR receptors; this effect has been previously observed and characterized by our group.[3a,10]

Optical imaging of single labeled cells confirms the results obtained using spectrophotometry of cell suspensions (Figure 6). Both the bright-field and the dark-field imaging modalities show stronger contrast in the case of nanocluster labeled A-431 cells. Also, hyperspectral bright-field imaging revealed a much stronger absorbance in the red–NIR region of nanocluster labeled cells, compared to cells labeling with primary particles.

Since magneto-plasmonic nanoparticles can be advantageous in a number of emerging biomedical applications including magnetic capture and simultaneous PA detection of CTCs, we evaluated nanocluster performance with PA imaging in the red–NIR region where blood and biological tissues are more transparent. A series of PA images at multiple wavelengths were acquired from A-431 cancer cells labeled with anti-EGFR nanoclusters and primary 6 nm particles (**Figure 7**). The use of nanoclusters increased the strength of PA signal from labeled cells in the NIR region by more than 4 times as compared to primary particles (Figure 7D). This quality makes the nanoclusters an attractive agent for in vivo imaging where absorption from endogenous chromophores, such as hemoglobin is significantly reduced in the NIR region.[27]

Previously, we showed that primary 6 nm magneto-plasmonic nanoparticles can be used for magnetic capture of cancer cells spiked in whole blood.[9a] Here, we compared the performance of primary particles with magneto-plasmonic nanoclusters. The same molar concentration of either anti-EGFR antibody conjugated primary particles or targeted nanoclusters were used to label the same amount of A-431 cells. Then, labeled cells were placed in a 1 cm cuvette with a permanent

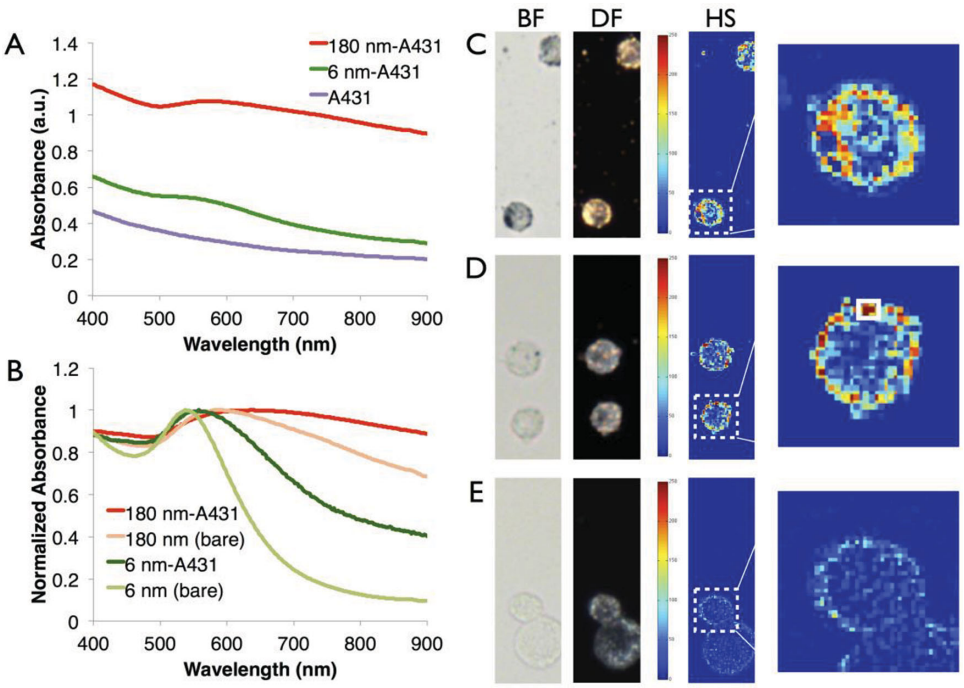

Figure 6. Optical properties of cells labeled with molecular targeted nanoparticles. (A, B) UV-Vis spectra of A-431 cells labeled with either EGFR-targeted primary particles or nanoclusters using the same mass of Au: A) raw spectra, and B) absorbance spectra of the labeled cells normalized to one after subtraction of the cell only spectrum in comparison with spectra from nanoparticle suspensions. C–E) Optical properties of individual A-431 cells labeled with EGFR-targeted nanoclusters (C) or primary particles (D). The unlabeled cells are shown as a control (E). Columns from left to right: bright field (BF); dark field (DF); and hyperspectral absorbance (HS) images. The color bars show relative intensity distribution in the HS images for an integrated absorbance from 500 to 700 nm.

magnet positioned on one side (similar to the set-up shown in Figure 3B,C). The efficiency of cell separation was determined by comparing the amount of magnetically-trapped cells and cells in a control cuvette without a magnet:

$$\left(1-\frac{\text{cell count from magnet treated sample}}{\text{cell count from control(no magnet)}}\right)\times 100\%$$

The results demonstrate enhanced magnetic cell separation by nanoclusters at shorter time periods (**Figure 8**), which is a key improvement because there is a critical need for development of faster CTC assays, especially in point-of-care applications. The capture yield of nanoclusters achieved ≈93% after a 10 min magnetic incubation while the primary particles showed just ≈70% capture efficiency at this time point. Hence, immunotargeted nanoclusters provide a more efficient agent for molecular specific magnetic separation of cells of interests.

3. Conclusions

Here, we used oil-in-water microemulsion method to create novel magneto-plasmonic nanoparticles with enhanced magnetic and plasmonic functionalities. The unique feature of our method is the formation of the hybrid nanostructures from ≈6 nm primary building blocks with magneto-plasmonic properties. We demonstrated that the choice of the right surfactant in synthesis of the magneto-plasmonic nanoclusters and subsequent surface modification with mPEG molecules are both important steps in producing biocompatible nanoclusters, which do not exhibit cytotoxic properties. The nanoclusters show a greatly improved response to an external magnetic field when compared to the constituent primary particles. In addition, the nanoclusters have a strong NIR absorbance that is absent in the primary particles. The outer gold surface of the nanoclusters can be easily modified with antibody molecules using thiolated linkers. Cancer cells labeled with targeted magneto-plasmonic nanoclusters produce a strong PA signal in the red–NIR region that can be used for sensitive molecular imaging. Furthermore, the labeled cells can be efficiently captured using an external magnetic field. Therefore, these biocompatible magneto-plasmonic nanostructures can enable the development of many biomedical applications, including multimodal molecular imaging, cell tracking, highly efficient assays for simultaneous capture and enumeration of circulating cancer cells, and cell magnetic guidance under imaging monitoring.

4. Experimental Section

Synthesis of Nanoclusters: Oleic acid-capped Au shell/ iron oxide core primary nanoparticles were synthesized according to a previously published method.[28] Briefly, 1 mmol iron(III) acetylacetonate was mixed in 10 mL of phenyl ether, followed by addition of 2 mmol oleic acid, 2 mmol oleylamine, and 5 mmol 1,2-hexadecanediol. The mixture was stirred and heated to 260 °C for 1 h under reflux. Then, 5 mL of as synthetized Fe_3O_4 nanoparticles was mixed with 1.1 mmol gold acetate,

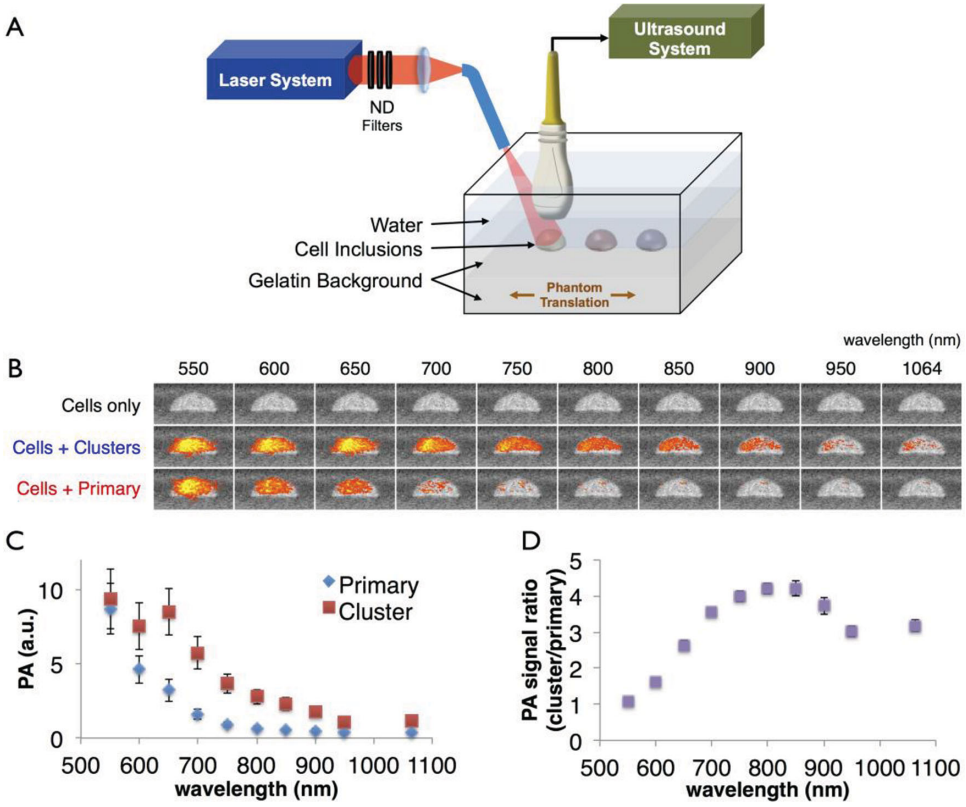

Figure 7. Photoacoustic imaging of labeled A-431 cells in tissue-mimicking cell phantoms. The cells were labeled with either EGFR-targeted nanoclusters or primary particles using the same mass of Au during labeling. A) Schematic of the experimental setup for combined ultrasound and photoacoustic imaging. B) Combined ultrasound and photoacoustic images of cell phantoms: unlabeled cells (top row), nanocluster labeled cells (middle row), and primary particles labeled cells (bottom row). C) A plot of un-normalized PA signal intensity integrated over cell inclusions in the phantom as a function of wavelength. D) The ratio of PA signal intensities from nanocluster labeled cells to primary particles labeled cells as a function of wavelength.

0.75 mmol oleic acid, 3 mmol oleylamine, 3 mmol 1,2-hexadecanediol, and 15 mL of phenyl ether under vigorous stirring. The reaction mixture was heated to 180 °C for 1 h under reflux. A dark purple precipitate was formed after addition of ethanol and centrifugation. The synthesis resulted in primary magneto-plasmonic particles with ≈6 nm diameter that were dispersed in hexane. To make nanoclusters, one volume of a suspension of the primary particles (5 mg/mL by total weight) in hexane was mixed with ten volumes of deionized water containing an anionic surfactant—sodium dodecyl sulfate (SDS, Sigma) at 2.8 mg/mL.[14b] The mixture was placed in a sonicator bath (Model 1510, Branson) for 2 h. After starting the sonication, the solution was shaken by hand gently to facilitate mixing between the phase containing primary hybrid nanoparticles and the bottom aqueous phase. After sonication, the solution was heated in a water bath at 80 °C for 10 min to remove hexane. As synthetized nanoclusters have a wide size distribution. Nanoclusters with various sizes were separated using the following sequence of centrifugation steps: first, nanoclusters with sizes ≈180 nm were collected by centrifugation at 100 × *g* for 30 min; then, ≈130 nm size was separated from the residual suspension applying the force of 400 × *g* for 30 min; and ≈90 nm size was recovered using 1500 × *g* for 30 min. Primary iron oxide core gold shell nanoparticles were transferred to an aqueous phase as previously described.[9a] Briefly, the nanoparticles in hexane at ≈0.6 mg/mL were mixed with an equal volume of deionized water containing 5 mM α-cyclodextrin and were stirred overnight at room temperature. Then, the nanoparticles were recovered by centrifugation at 3250 × *g* for 30 min and were resuspended in 0.2 mM sodium citrate under 10 min sonication.

Characterization of Nanoclusters: The size and morphology of nanoclusters were examined using a FEI TECNAI G2 F20 X-TWIN TEM at 80 keV, and FEI Quanta 650 SEM. Ultraviolet-visible-NIR (UV-Vis-NIR) absorbance spectra were collected with a BioTek Synergy HT micro-titer plate spectrophotometer. Magnetization curves were analyzed using SQUID magnetometry upon cycling the magnetic field from − 10 K Oe to 10 K Oe at 300 K. A DelsaNano (Beckman Coulter) was used to determine zeta potentials of the nanoparticles. The response of the bare particles to a magnetic field as a function of time was characterized by placing a cubic magnet (1 cm × 1cm × 1 cm, NdFeB, K&J Magnetics) next to one side of a 1 cm cuvette loaded with nanoparticles, followed by measurements of UV-Vis spectra from the colloidal suspension over time.

Cell Viability Assay: A431 cells (5 × 10^3 cells) were incubated with SDS-capped clusters, CTAB (Cetyltrimethylammonium Bromide)-capped clusters, or PEG-capped clusters (particle concentration = 0.05 nM, sterilized by passing through 0.45 μm filter) in a phenol-free DMEM cell culture media supplemented with 5% FBS for 8 h at 37 °C. The cells incubated with nanoclusters and the untreated cell control were then washed twice with PBS and mixed with 100 μL MTS reagent, a mixture of MTS (3-(4,5-dimethylthiazol-2-yl)-5-(3-carboxymethoxyphenyl)-2-(4-sulfophenyl)-2H-tetrazolium) (0.32 mg/mL, Promega) and PMS (phenazine methosulfate) (7.3 μg/mL, Sigma) in cell culture media. Absorbance at 490 nm was taken 3 h after the addition of the MTS reagent using a BioTek Synergy HT micro-titer plate spectrophotometer; the absorbance is proportional to the number of metabolically active live cells in a sample.

Antibody Conjugation to Nanoclusters: The carbohydrate moiety on the Fc portion of monoclonal IgG antibodies—anti-Epidermal Growth Factor Receptor 2 (HER2) antibody (E2777, Sigma) and anti-Epidermal Growth Factor Receptor 1 (EGFR) antibody (E2156, Sigma)—were

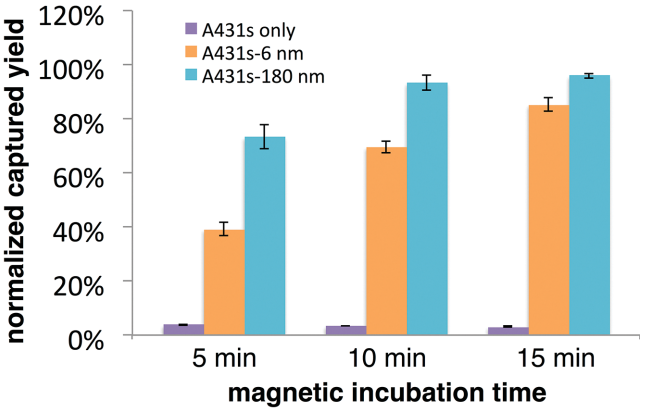

Figure 8. Magnetic capture efficiency as a function of time for A-431 cells labeled with either EGFR-targeted primary particles or nanoclusters. The experiment was carried out using the same approach as shown in Figures 3B,C. The bar graph shows a capture yield that was calculated as following: (1 – ([number of cells in suspension at a given time]/[number of cells before incubation with a magnet])) × 100%.

thiolated following our previously published protocol.[17] Briefly, 10 µL of 100 mM $NaIO_4$ was added to 100 µl of monoclonal antibody solution (1 mg/mL) in pH 7.2 HEPES for 30 min under dark conditions. The reaction was quenched with 500 µL of 1× PBS. Then, 2 µl of 46.5 mM heterobifunctional polyethylene glycol linker solution (dithiolaromatic PEG6-CONHNH2, SensoPath Inc.) was mixed with the antibody solution for 1 h at room temperature. The linker modified antibodies were purified using a 10k MWCO centrifuge filter at 3250 × *g* for 20 min at 8 °C. Then, the modified antibodies (1 µL at 1 mg/mL) were mixed with the nanoclusters (100 µL at O.D. 1) for 2 hours at room temperature. Finally, 10 µL of 10^{-3} M 5 kDa mPEG-SH (SensoPath Technologies) was added to the mixture to replace any residual SDS molecules from the surface of nanoclusters. The functionalized nanoclusters were recovered by centrifugation at 830 × *g* for 3 min, and were resuspended in 100 uL 2% w/v 5 kDa PEG in PBS. Conjugation of antibodies to primary iron oxide core/gold shell nanoparticles was carried out by mixing the linker modified antibodies (1 µL at 1 mg/mL) with the particles (100 µL at O.D. 2) for 2 h at room temperature. Then, 10 µL of 10^{-3} M 5 kDa mPEG-SH was added to the mixture for 20 min on a shaker. The functionalized primary nanoparticles were recovered by centrifugation at 3320 × *g* for 3 min and were resuspended in 100 µL 2% (w/v) 5 kDa PEG in PBS.

Cell Labeling Specificity Test: Cancer cells SK-BR-3 and A-431 (ATCC) were cultured in Dulbecco's Modified Eagle Medium (DMEM, Gibco) supplemented with 5% fetal bovine serum (FBS, Hyclone). Before labelling with nanoclusters, cells were harvested at ≈90% confluence using trypsin and resuspended in 1 mL complete media containing ≈5 × 10^5 cells. Nanoclusters (0.05 nM) conjugated with either anti-HER2 or anti-EGFR antibodies were mixed with a cell suspension for 2 h at room temperature under mild shaking. After incubation with nanoclusters, cells were washed from any unbound particles via centrifugation at 182 × *g* for 3 min and were resuspended in a phosphate buffered saline. Then, dark field images of the cells were obtained under Leica DM6000 upright microscope using 20×, 0.5-NA dark field objective and a Xe-lamp illumination.

Hyperspectral Imaging: Hyperspectral images were acquired in bright-field transmittance mode under Leica DM600 upright microscope equipped with a PARISS spectral imager (Lightform, Inc.) using a 20×, 0.5-NA objective and a 100 W halogen light source. The wavelength calibration was carried out using a standard low pressure Hg wavelength calibration lamp (Lightform). The hyperspectral images of cells were normalized by a spectrum obtained from a region without cells.

Photoacoustic Imaging: Photoacoustic imaging experiments were carried out using tissue-mimicking ultrasonic phantoms.[29] First, a 5 cm thick base-layer was prepared using 8% gelatin, 0.25% 40-µm silica particles, and 0.1% formaldehyde.[30] Then, cell inclusions were made by mixing 7.5 µL of gelatin (16% gelatin, 0.5% 40-µm silica particles, and 0.2% formaldehyde) with 7.5 µL of formalin fixed pre-labeled A431 cells. The inclusions contained ≈100 000 cells and were pipetted onto the surface of the base-layer. After curing for 1 hour at 4 °C, the same procedure used to make the base layer was utilized to make a 1 cm thick layer on top of cell inclusions. Cell phantoms were imaged using a Vevo 2100 (VisualSonics Inc.) for the photoacoustic signal acquisition and a Quanta-Ray PRO-290 pumping a premiScan/MB tunable OPO (Spectra-Physics Lasers) for the photoacoustic excitation. For photoacoustic images acquired using wavelengths shorter than 710 nm, the laser beam from the signal port of the OPO was coupled into an Optran WF multimode optical fiber (CeramOptec Industries, Inc.). The diameter of the laser spot on the surface of the phantom was 1 cm and the fluence was maintained at 3 mJ/cm^2 for all wavelengths using an array of neutral density (ND) filters. The 21 MHz transducer of the Vevo 2100 was positioned orthogonal to the surface of the phantom (as shown in Figure 7A) and was used to acquire the photoacoustic signals resulting from the nanosecond laser pulses. Photoacoustic images were acquired at 550 nm, 600 nm, 650 nm, and 700 nm with the optical fiber and ultrasound transducer being stationary and the phantom moving so that a single inclusion with either labeled or unlabeled A431 cells was in the imaging plane. After the photoacoustic images were acquired the laser source was switched from the signal port to the idler port of the OPO. The phantom was repositioned and photoacoustic images were acquired at 750 nm, 800 nm, 850 nm, 900 nm, 950 nm, and 1064 nm wavelengths. An average of 50 photoacoustic images were obtained at each wavelength (see Figure 7B). The photoacoustic signal intensity from a small region of interest (3 mm by 3 mm) in the phantom was averaged and plotted as a function of wavelength (Figure 7C).

Magnetic Capture Efficiency Test: A-431 cells in culture medium (5 × 10^5 cells) were labeled with either anti-EGFR conjugated primary particles or nanoclusters (both at the concentration of 0.05 nM) for 1 h at room temperature. After labeling, A-431 cells were washed with 1× PBS. The labeled cells were then resuspended in 1 mL of 1× PBS and placed into a 1 cm cuvette. A cubic magnet (1 cm × 1 cm × 1 cm, NdFeB, K&J Magnetics) was positioned next to the cuvette's wall, and a 10 µL sample was taken from the center of the cuvette at time points 5 min, 10 min, and 15 min.

Supporting Information

Supporting Information is available from the Wiley Online Library or from the author.

Acknowledgements

This work was supported by the National Institute of Health under grants R01 EB008101 and R01 CA103830.

Received: June 3, 2014
Revised: July 14, 2014
Published online: September 1, 2014

[1] a) L. K. Bogart, G. Pourroy, C. J. Murphy, V. Puntes, T. Pellegrino, D. Rosenblum, D. Peer, R. Levy, *ACS Nano* **2014**, *8*, 3107–3122; b) T. L. Doane, C. Burda, *Chem. Soc. Rev.* **2012**, *41*, 2885–2911.
[2] a) E. C. Dreaden, A. M. Alkilany, X. Huang, C. J. Murphy, M. A. El-Sayed, *Chem. Soc. Rev.* **2012**, *41*, 2740–2779; b) M. Colombo, S. Carregal-Romero, M. F. Casula, L. Gutierrez, M. P. Morales, I. B. Bohm, J. T. Heverhagen, D. Prosperi, W. J. Parak, *Chem. Soc. Rev.* **2012**, *41*, 4306–4334.
[3] a) K. Sokolov, M. Follen, J. Aaron, I. Pavlova, A. Malpica, R. Lotan, R. Richards-Kortum, *Cancer Res.* **2003**, *63*, 1999–2004; b) S. Mallidi,

T. Larson, J. Aaron, K. Sokolov, S. Emelianov, *Opt. Express* **2007**, *15*, 6583–6588; c) P. K. Jain, X. Huang, I. H. El-Sayed, M. A. El-Sayed, *Acc. Chem. Res.* **2008**, *41*, 1578–1586; d) F. Ratto, P. Matteini, F. Rossi, L. Menabuoni, N. Tiwari, S. K. Kulkarni, R. Pini, *Nanomedicine* **2009**, *5*, 143–151; e) L. R. Hirsch, R. J. Stafford, J. A. Bankson, S. R. Sershen, B. Rivera, R. E. Price, J. D. Hazle, N. J. Halas, J. L. West, *Proc. Natl. Acad. Sci. U.S.A.* **2003**, *100*, 13549–13554; f) M. J. Crow, G. Grant, J. M. Provenzale, A. Wax, *Am. J. Roentgenol.* **2009**, *192*, 1021–1028; g) Y. Choi, T. Kang, L. P. Lee, *Nano Lett* **2009**, *9*, 85–90; h) S. E. Lee, D. Y. Sasaki, Y. Park, R. Xu, J. S. Brennan, M. J. Bissell, L. P. Lee, *ACS Nano* **2012**, *6*, 7770–7780; i) A. Wax, K. Sokolov, *Laser Photonics Rev.* **2009**, *3*, 146–158.

[4] a) Y. Jing, L. R. Moore, P. S. Williams, J. J. Chalmers, S. S. Farag, B. Bolwell, M. Zborowski, *Biotechnol. Bioeng.* **2007**, *96*, 1139–1154; b) M. Qu, S. Mallidi, M. Mehrmohammadi, R. Truby, K. Homan, P. Joshi, Y.-S. Chen, K. Sokolov, S. Emelianov, *Biomed. Opt. Express* **2011**, *2*, 385–396; c) C. Sun, J. S. Lee, M. Zhang, *Adv. Drug Delivery Rev.* **2008**, *60*, 1252–1265; d) A. Ito, Y. Kuga, H. Honda, H. Kikkawa, A. Horiuchi, Y. Watanabe, T. Kobayashi, *Cancer Lett.* **2004**, *212*, 167–175; e) Q. A. Pankhurst, J. Connolly, S. K. Jones, J. Dobson, *J. Phys. D: Appl. Phys.* **2003**, *36*, R167.

[5] a) T. A. Larson, J. Bankson, J. Aaron, K. Sokolov, *Nanotechnology* **2007**, *18*, 325101; b) J. Aaron, N. Nitin, K. Travis, S. Kumar, T. Collier, S. Y. Park, M. Jose-Yacaman, L. Coghlan, M. Follen, R. Richards-Kortum, K. Sokolov, *J. Biomed. Opt.* **2007**, *12*, 034007; c) H.-M. Song, Q. Wei, Q. K. Ong, A. Wei, *ACS Nano* **2010**, *4*, 5163–5173.

[6] J. S. Aaron, J. Oh, T. A. Larson, S. Kumar, T. E. Milner, K. V. Sokolov, *Opt. Express* **2006**, *14*, 12930–12943.

[7] Y. Jin, C. Jia, S.-W. Huang, M. O'Donnell, X. Gao, *Nat. Commun.* **2010**, *1*, 41.

[8] E. I. Galanzha, E. V. Shashkov, T. Kelly, J.-W. Kim, L. Yang, V. P. Zharov, *Nat. Nanotechnol.* **2009**, *4*, 855–860.

[9] a) C.-H. Wu, Y.-Y. Huang, P. Chen, K. Hoshino, H. Liu, E. P. Frenkel, J. X. J. Zhang, K. V. Sokolov, *ACS Nano* **2013**, *7*, 8816–8823; b) X. Hu, C. W. Wei, J. Xia, I. Pelivanov, M. O'Donnell, X. Gao, *Small* **2013**, *9*, 2046–2052.

[10] a) J. Aaron, N. Nitin, K. Travis, S. Kumar, T. Collier, S. Y. Park, M. Jose-Yacaman, L. Coghlan, M. Follen, R. Richards-Kortum, K. Sokolov, *J. Biomed. Opt.* **2007**, *12*, 034007; b) J. Aaron, K. Travis, N. Harrison, K. Sokolov, *Nano Lett.* **2009**, *9*, 3612–3618.

[11] a) H. Wang, D. W. Brandl, F. Le, P. Nordlander, N. J. Halas, *Nano Lett.* **2006**, *6*, 827–832; b) L. Wang, J. Bai, Y. Li, Y. Huang, *Angew. Chem. Int. Ed.* **2008**, *47*, 2439–2442.

[12] a) L. L. Ma, M. D. Feldman, J. M. Tam, A. S. Paranjape, K. K. Cheruku, T. A. Larson, J. O. Tam, D. R. Ingram, V. Paramita, J. W. Villard, J. T. Jenkins, T. Wang, G. D. Clarke, R. Asmis, K. Sokolov, B. Chandrasekar, T. E. Milner, K. P. Johnston, *ACS Nano* **2009**, *3*, 2686–2696; b) L. L. Ma, J. O. Tam, B. W. Willsey, D. Rigdon, R. Ramesh, K. Sokolov, K. P. Johnston, *Langmuir* **2011**, *27*, 7681–7690.

[13] L. L. Ma, A. U. Borwankar, B. W. Willsey, K. Y. Yoon, J. O. Tam, K. V. Sokolov, M. D. Feldman, T. E. Milner, K. P. Johnston, *Nanotechnology* **2013**, *24*, 025606.

[14] a) P. Qiu, C. Jensen, N. Charity, R. Towner, C. Mao, *J. Am. Chem. Soc.* **2010**, *132*, 17724–17732; b) F. Bai, D. Wang, Z. Huo, W. Chen, L. Liu, X. Liang, C. Chen, X. Wang, Q. Peng, Y. Li, *Angew. Chem. Int. Ed.* **2007**, *46*, 6650–6653.

[15] R. Qiao, C. Yang, M. Gao, *J. Mater. Chem.* **2009**, *19*, 6274–6293.

[16] a) S. Maheswaran, L. V. Sequist, S. Nagrath, L. Ulkus, B. Brannigan, C. V. Collura, E. Inserra, S. Diederichs, A. J. Iafrate, D. W. Bell, S. Digumarthy, A. Muzikansky, D. Irimia, J. Settleman, R. G. Tompkins, T. J. Lynch, M. Toner, D. A. Haber, *N. Engl. J. Med.* **2008**, *359*, 366–377; b) D. J. Slamon, B. Leyland-Jones, S. Shak, H. Fuchs, V. Paton, A. Bajamonde, T. Fleming, W. Eiermann, J. Wolter, M. Pegram, J. Baselga, L. Norton, *N. Engl. J. Med.* **2001**, *344*, 783–792.

[17] S. Kumar, J. Aaron, K. Sokolov, *Nat. Protoc.* **2008**, *3*, 314–320.

[18] L. Wang, L. Wang, J. Luo, Q. Fan, M. Suzuki, I. S. Suzuki, M. H. Engelhard, Y. Lin, N. Kim, J. Q. Wang, *J. Phys. Chem. B* **2005**, *109*, 21593–21601.

[19] P. K. Jain, K. S. Lee, I. H. El-Sayed, M. A. El-Sayed, *J. Phys. Chem. B* **2006**, *110*, 7238–7248.

[20] K. Kneipp, H. Kneipp, I. Itzkan, R. R. Dasari, M. S. Feld, M. S. Dresselhaus, in *Optical properties of nanostructured random media*, Springer, **2002**, pp 227–249.

[21] a) S. Kumar, N. Harrison, R. Richards-Kortum, K. Sokolov, *Nano Lett.* **2007**, *7*, 1338–1343; b) B. Khlebtsov, V. Zharov, A. Melnikov, V. Tuchin, N. Khlebtsov, *Nanotechnology* **2006**, *17*, 5167; c) G. A. DeVries, M. Brunnbauer, Y. Hu, A. M. Jackson, B. Long, B. T. Neltner, O. Uzun, B. H. Wunsch, F. Stellacci, *Science* **2007**, *315*, 358–361.

[22] U. Kreibig, M. Vollmer, *Optical properties of metal clusters*, Springer, Berlin; New York **1995.**

[23] C. H. Su, H. S. Sheu, C. Y. Lin, C. C. Huang, Y. W. Lo, Y. C. Pu, J. C. Weng, D. B. Shieh, J. H. Chen, C. S. Yeh, *J. Am. Chem. Soc.* **2007**, *129*, 2139–2146.

[24] A. M. Alkilany, P. K. Nagaria, C. R. Hexel, T. J. Shaw, C. J. Murphy, M. D. Wyatt, *Small* **2009**, *5*, 701–708.

[25] P. P. Joshi, S. J. Yoon, W. G. Hardin, S. Emelianov, K. V. Sokolov, *Bioconj. Chem.* **2013.**

[26] A. Rath, M. Glibowicka, V. G. Nadeau, G. Chen, C. M. Deber, *Proc. Natl. Acad. Sci.* **2009**, *106*, 1760–1765.

[27] S. Y. Emelianov, P. C. Li, M. O'Donnell, *Phys. Today* **2009**, *62*, 34–39.

[28] Z. Xu, Y. Hou, S. Sun, *J. Am. Chem. Soc.* **2007**, *129*, 8698–8699.

[29] S. J. Yoon, S. Mallidi, J. M. Tam, J. O. Tam, A. Murthy, K. P. Johnston, K. V. Sokolov, S. Y. Emelianov, *Opt. Lett.* **2010**, *35*, 3751–3753.

[30] J. R. Cook, R. R. Bouchard, S. Y. Emelianov, *Biomed. Opt. Express* **2011**, *2*, 3193–3206.